Vacuum 230 (2024) 113651

Contents lists available at ScienceDirect

Vacuum

journal homepage: www.elsevier.com/locate/vacuum

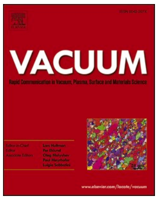

Effect of Y on the microstructure and physical properties of Cu-Zr-Mg-Y alloys

Haoyan Hu [a], Meng Zhou [a,**], Xu Li [b], Yi Zhang [a,*], Qian Bai [c,***], Bo Yang [a], Jin Zou [d], Ke Jing [a], Zheng'ao Li [a], Gang'ao Xin [a], Baohong Tian [a], Alex A. Volinsky [e]

[a] *Henan University of Science and Technology, School of Materials Science and Engineering, Provincial and Ministerial Co-construction of Collaborative Innovation Center for Non-ferrous Metals New Materials and Advanced Processing Technology, Henan Province, Luoyang, 471023, PR China*
[b] *Center for Advanced Measurement Science, National Institute of Metrology, Beijing, 100029, PR China*
[c] *Medical Research Center, The Second Affiliated Hospital of Zhengzhou University, Zhengzhou, 450014, PR China*
[d] *Jiangxi Key Laboratory for Advanced Copper and Tungsten Materials, Jiangxi Academic of Sciences, Nanchang, 330096, PR China*
[e] *Department of Mechanical Engineering, University of South Florida, 4202 E. Fowler Ave. ENG 030, Tampa, 33620, USA*

ARTICLE INFO

Handling Editor: Prof. L.G. Hultman

Keywords:
Cu-Zr-Mg-Y alloy
Precipitates
Microstructure evolution
Mechanical properties

ABSTRACT

This work presents the development of two novel Cu-Zr-Mg(Y) alloys. The alloys were prepared using vacuum melting and show good conductivity and mechanical properties after solution treatment+60 % cold rolling + aging at 450 °C for 60 min.

The measurement results reveal that the Cu-Zr-Mg alloy has a microhardness of 165 ± 5 HV, an electrical conductivity of 68.5 ± 0.2 % IACS and a tensile strength of 483 ± 15 MPa while the Cu-Zr-Mg-Y alloy has a microhardness of 172 ± 6 HV, an electrical conductivity of 67.9 ± 0.2 % IACS and a tensile strength of 503 ± 12 MPa.

The addition of Y promotes the recovery and recrystallization of the alloys and causes the refinement of the grain size. The appearance of copper texture is the reason why the Cu-Zr-Mg-Y alloy has higher tensile strength in the rolling direction. The main phases of the Cu-Zr-Mg-Y alloy consist of Cu_5Zr and a small amount of $Mg_{24}Y_5$. The increment in precipitation strengthening is primarily attributed to the coherent Cu_5Zr phase within the matrix.

1. Introduction

Copper and its alloys exhibit exceptional mechanical properties and electrical conductivity, rendering them optimal materials for lead frames. In recent decades, the development of copper-based alloys has received extensive attention [1], notable developments include Cu-Fe-P [2–4], Cu-Cr [5,6], Cu-Ti [7,8], Cu-Ni-Si [9,10], Cu-Cr-Zr [11], Cu-Zr [12], etc. Relevant studies demonstrate that the incorporation of alloy elements can significantly enhance the strength of the material; however, it often induces lattice distortion, augments electron scattering, and diminishes conductivity [13]. Among age-hardening alloys, Cu-Zr alloys demonstrate significant age-strengthening capability while minimally impacting electrical conductivity.

From Fig. 1(a) [14], compared to other alloying elements, Zr exhibits a lesser impact on the electrical conductivity of Cu alloys. The solubility of Zr in copper is limited at room temperature (only 0.01 %, as shown in Fig. 1(b)), minimizes electron scattering, making the alloy ideal for electronic devices [15–18]. Currently, the primary research focus on Cu-Zr alloys lies in enhancing their mechanical properties through strategies such as optimizing Zr content, promoting solid solution formation, and incorporating additional alloying elements. Azimi et al. [19] studied the influence of mechanical alloying on the solid solubility of Zr in the matrix and found that mechanical alloying can significantly improve the solid solubility of Zr in Cu. Kimura et al. [20] investigated the impact of cold drawing on the electrical and mechanical characteristics of Cu-5at% Zr alloy, noting improved conductivity and strength. Deng et al. [21] investigated the Cu-Cr-Zr alloy, the main phases of the alloy are Cr and Cu_5Zr. It was found that Cr facilitates the precipitation

---

* Corresponding author.
** Corresponding author.
*** Corresponding author.

E-mail addresses: zhoumeng0902@126.com (M. Zhou), zhshgu436@163.com (Y. Zhang), baiqian@zzu.edu.cn (Q. Bai).

https://doi.org/10.1016/j.vacuum.2024.113651
Received 9 February 2024; Received in revised form 11 September 2024; Accepted 13 September 2024

of Cu_5Zr, while Zr refines the precipitation of Cr.

In this study, we choose to increase the content of Zr and add more elements. When the Zr mass fraction reaches 1.2 %, the presence of excess phase significantly enhances the mechanical properties of the alloy. We chose to include the Mg element with the aim of improving the alloy's mechanical characteristics. Despite the challenges associated with incorporating Mg during the melting process, numerous studies have consistently demonstrated that the addition of Mg can significantly enhance the mechanical properties of the alloy [22–27]. While rare earth element Y has the potential to enhance matrix purification, grain refinement, and mechanical properties, it may also result in a slight reduction in conductivity [28]. The present study investigates the influence of Y on the microstructure, mechanical properties, and electrical properties of the alloy. So Cu-1.2Zr-0.3 Mg and Cu-1.2Zr-0.3Mg-0.15Y alloys were prepared.

In terms of melting method, vacuum melting is an effective method to prevent alloy oxidation and improve alloy quality [29–32]. Chen et al. [33] prepared Cu-Cr-C alloy by vacuum melting. SEM observation showed that the interface between the two phases was clear without obvious impurities. Abiko et al. [34] smelted ultra pure iron using ultra-high vacuum melting technology, and found that this technology is very useful for the reduction of gaseous impurities.Because Zr, Mg and Y are easily oxidized, we choose vacuum melting to prepare the alloy to ensure the quality of the alloy.

The optimal aging process of Cu-Zr-Mg (Y) alloy was investigated, with a focus on elucidating the influence of Y on the alloy's aging properties. The heat treatment processes of solid solution, cold rolling, and aging for Cu-Zr-Mg and Cu-Zr-Mg-Y alloys were thoroughly examined, leading to the determination of optimal parameters for the aging process. The microstructure and strengthening mechanism of the alloy were investigated using transmission electron microscopy (TEM), backscattered electron diffraction (EBSD), and scanning electron microscopy (SEM). The microhardness and electrical conductivity differences between the two alloys were compared, and the impact of incorporating rare earth element Y on the strength and electrical conductivity of Cu-Zr-Mg-Y alloy was investigated.

2. Material and method

In this study, Cu-Zr-Mg and Cu-Zr-Mg-Y alloys were prepared using raw materials that included electrolytic cathode copper, pure Mg, pure Y, and a Cu-10 % Zr intermediate. In order to facilitate the mixing and melting process, the raw materials were chopped into small pieces.

The alloy is melted and prepared in zg-0.01-40-4 medium frequency vacuum induction melting furnace, and the casting process is carried out in argon atmosphere. First, the cut material is put into the furnace, and the vacuum is pumped to about 14 Pa through mechanical pump and rotary vane pump, and then argon gas is slowly added as the protective gas to make the pressure in the furnace stable at 20000 Pa. The current is slowly increased until the block is completely melted, and the melt is mixed evenly through mechanical stirring, and the casting is made after melting for 20–30 min.After the cast sample is allowed to cool inside the furnace for 1 h, air is introduced to gradually return the pressure to normal. Once the pressure stabilizes, the furnace door is opened, and the sample is removed.

After the ingot was cast and chilled to room temperature, to ensure the successful addition of Zr, Mg, and Y elements, we conducted composition testing on the melted alloy using ICP(Inductively Coupled Plasma) technology, and the results are shown in Table 1. Then the riser was cut off, and the surface was polished with sandpaper to remove the oxide scale. Subsequently, the ingot was annealed in the furnace at 900 °C for 1 h for heat treatment. The sample was then cut into pieces measuring 100 mm × 10 mm × 2 mm. These samples were put inside a vacuum heat treatment furnace for solid solution treatment at 930 °C for 1 h. Following this, cold rolling with a 60 % deformation was applied. Finally, the samples were aged at different temperatures (400–550 °C) and aging times (10–480 min). The experimental process is illustrated in Fig. 2.

The aged samples underwent polishing with sandpaper to eliminate the oxide scale. The electrical conductivity and microhardness of the two alloys were subsequently measured using an eddy current resistivity meter and an HVS-1000 microhardness tester, respectively. Five points are selected for each pattern to measure, and the results are averaged. After that, the tensile strength of the peak-aged alloy was tested. EBSD, TEM, and SEM were used for microstructure characterization.

For EBSD samples, rough polishing was conducted on a polishing machine. Subsequently, the samples were immersed in CH_3CH_2OH and H_3PO_4 solutions with 50 % content, respectively, and electropolished for 1 min under a voltage of 5 V. SEM and EBSD observations were performed using the ULTRATM55 scanning electron microscope. The TEM sample was prepared through mechanical polishing to a thickness of approximately 30 μm and then thinned using the Leica EM RES 101 ion thinner. Thinning parameters included an ion beam energy of 5 keV, ion gun angle of ±15° thinning to a hole, and 3 keV ± 5° thinning for 20 min. TEM observations were carried out using the LIBRA® 200 transmission electron microscope.

Table 1
Chemical composition of the Cu-Zr-Mg-(Y) alloys.

Alloy	Analyzed composition in wt.%			
	Zr	Mg	Y	Cu
Cu-1.2Zr-0.3 Mg	1.21	0.27	0	Bal.
Cu-1.2Zr-0.3Mg-0.15Y	1.16	0.28	0.15	Bal.

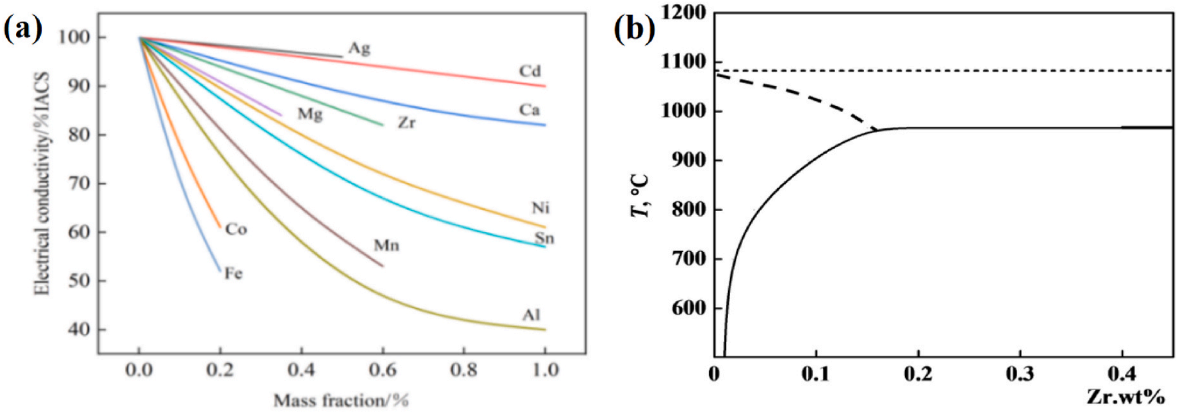

Fig. 1. (a) Relationship between elemental content and electrical conductivity of Cu alloy; (b) phase diagram of the Cu-Zr alloy.

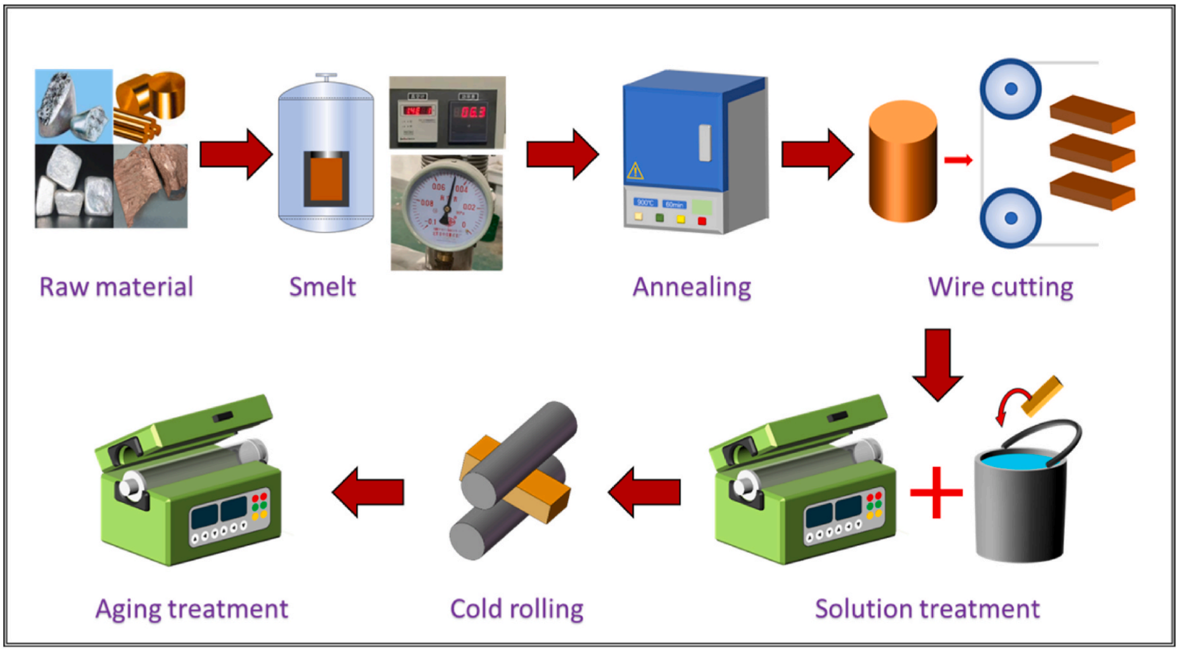

Fig. 2. An illustration of the experimental process.

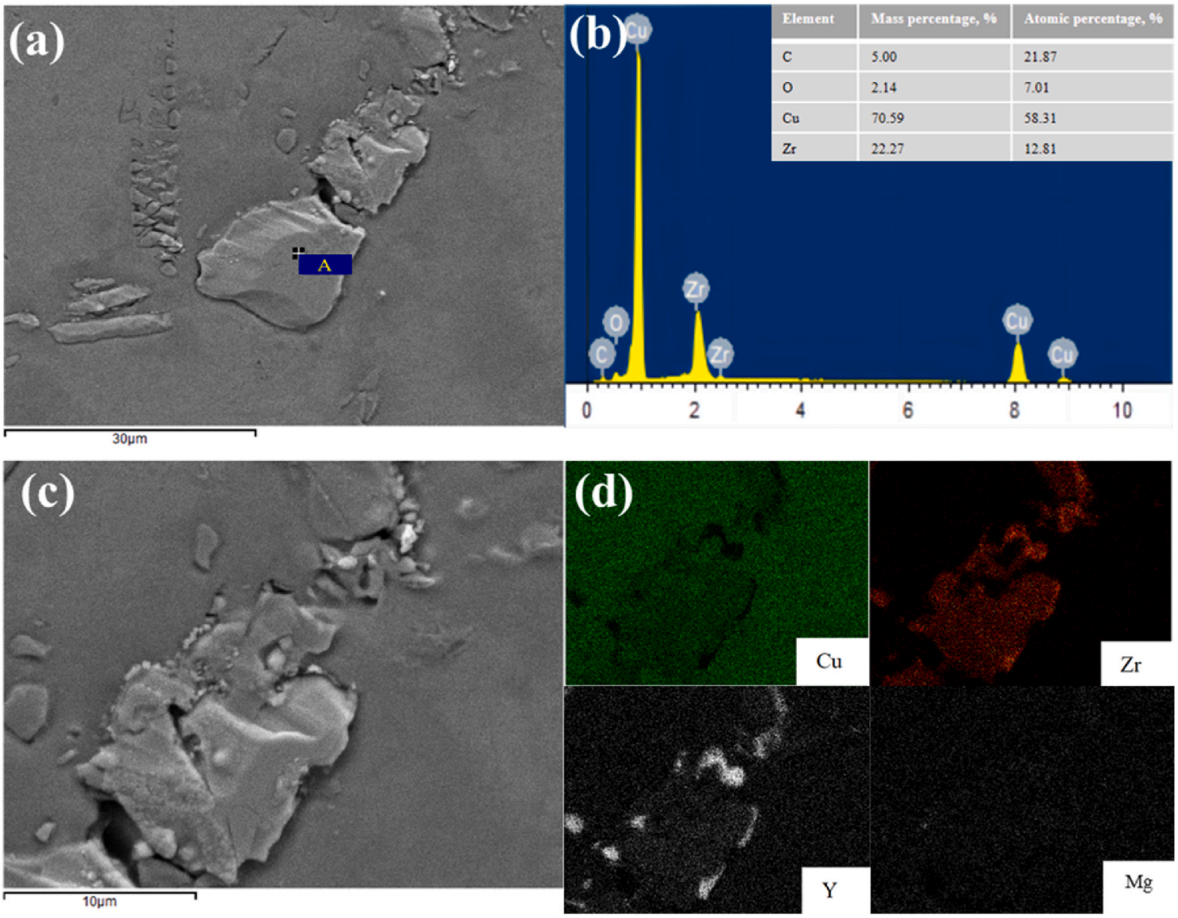

Element	Mass percentage, %	Atomic percentage, %
C	5.00	21.87
O	2.14	7.01
Cu	70.59	58.31
Zr	22.27	12.81

Fig. 3. SEM of Cu-Zr-Mg-Y alloy aged at 450 °C for 60 min: (a) (c) SEM images; (b) the energy spectrum of the points A in figure (a); (d) distribution diagram of main alloy elements.

3. Results

3.1. SEM analysis

Due to the limited solubility of Zr in Cu, a significant amount of undissolved secondary phases still persist following the process of solution treatment. To ascertain the composition and morphology of the excess phase, SEM analysis was conducted on the Cu-Zr-Mg-Y alloy, and the results are depicted in Fig. 3. It is evident from Fig. 3(a) and (c) that the size of the excess phase is approximately 10 μm. As revealed in Fig. 3 (b) and (d), the excess phase is identified as the Cu_5Zr phase. These granular excess phases impede dislocation movement, thereby enhancing the strength and microhardness of the alloy.

Furthermore, the clear manifestation of the Y element encircling Cu_5Zr can be observed in Fig. 3 (d). This arrangement hinders the growth of the excess phase to a certain extent, refines the size of the excess phase, and improves the alloy's strength and plasticity.

3.2. Mechanical properties and electrical conductivity

To determine the optimal aging parameters of the alloy and assess the effect of Y addition on the mechanical and electrical conductivity of the Cu-Zr-Mg-Y alloy, tests were conducted on the aging temperature and aging time of the two alloys. Measurements were taken for microhardness, electrical conductivity, and tensile strength, as illustrated in Fig. 4. To establish the optimal aging parameters for both alloys, the microhardness and electrical conductivity of the alloys were measured at different temperatures (400–550 °C) and aging times. Fig. 4(a)–(d) shows the results. Research has found that at the same temperature, with the extension of aging time, the microhardness of the alloy increases first and then decreases. At the early stage of aging, the amount of precipitates are limited, and the alloy is under-aging. During this phase, the microhardness increases rapidly and reaches its peak value, signifying the maximum contribution of precipitation strengthening by precipitates. Subsequently, as the alloy entered the over-aging stage, precipitates coarsen and grains begin to grow, resulting in a decline in microhardness over time. At the same aging time, the microhardness of the alloy also increased first and then decreased with the increase of temperature. At lower temperatures, the growth rate of precipitates is slow, and there is insufficient time for the formation of an adequate precipitation phase, resulting in inadequate precipitation strengthening and lower alloy microhardness. Conversely, at higher temperatures, precipitates tend to grow rapidly, diminishing the precipitation-strengthening effect. Simultaneously, accelerated recrystallization and grain growth lead to alloy softening. The conductivity of the two alloys increased with the increase of temperature and aging time. The alloy's ability to conduct electricity experienced a rapid increase at the onset of aging due to the precipitation of solid solution atoms and the reduction of dislocations and other defects. As most atoms precipitated, the rate of increase in electrical conductivity slowed, eventually stabilizing.

Fig. 5(a) illustrates the tensile strength curves of the two alloys at peak aging. The inclusion of Y greatly improves the alloy's resistance to tension. The optimal aging parameters for both alloys were determined to be aging at 450 °C for 60 min. At peak aging, the microhardness, electrical conductivity, and tensile strength of Cu-Zr-Mg alloy were 165 ± 5 HV, 68.5 ± 0.2 % IACS, and 483 ± 15 MPa, respectively.

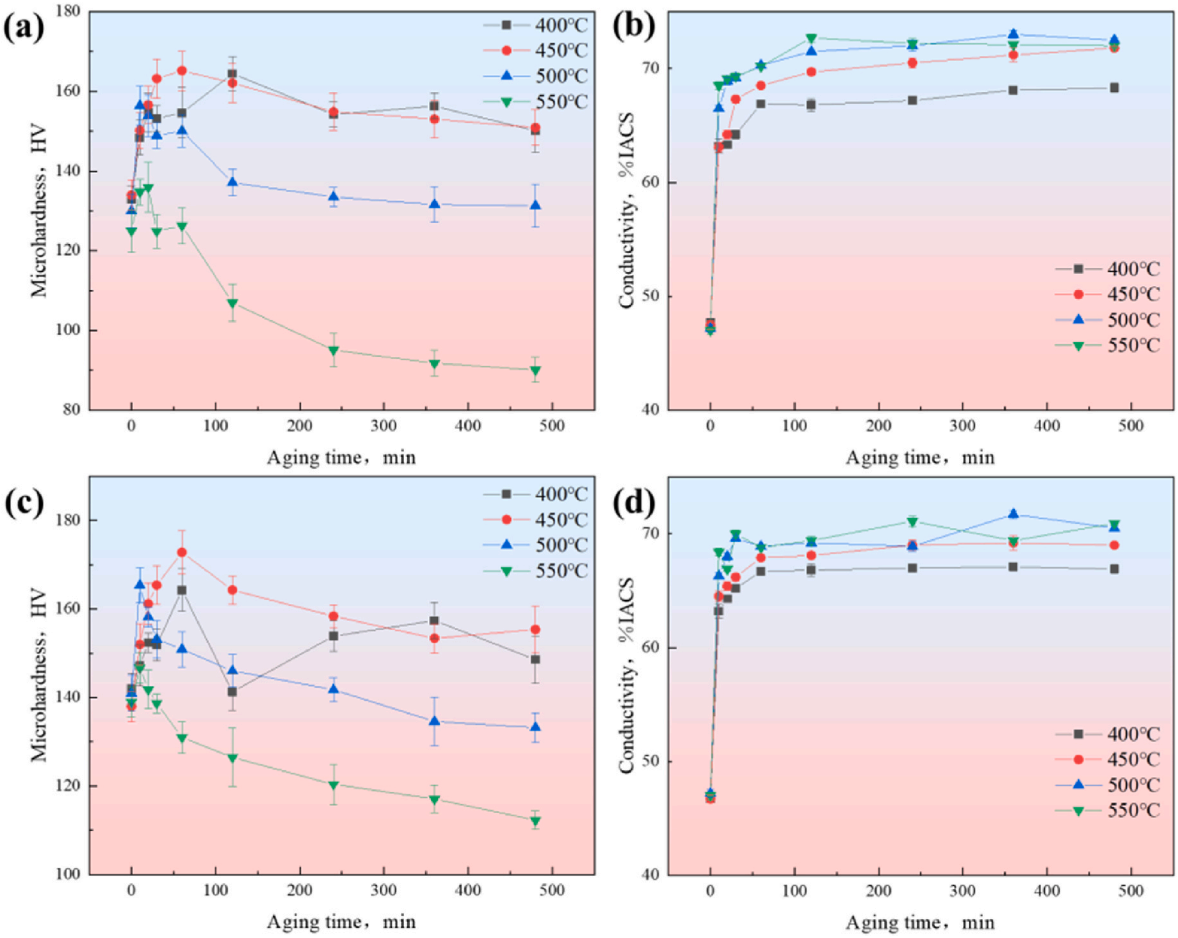

Fig. 4. Mechanical and electrical properties of Cu-Zr-Mg and Cu-Zr-Mg-Y: (a)(b) micro-hardness and electrical conductivity of Cu-Zr-Mg alloy aging at different temperatures and time; (c) (d) micro-hardness and electrical conductivity of Cu-Zr-Mg-Y alloy aging at different temperatures and time.

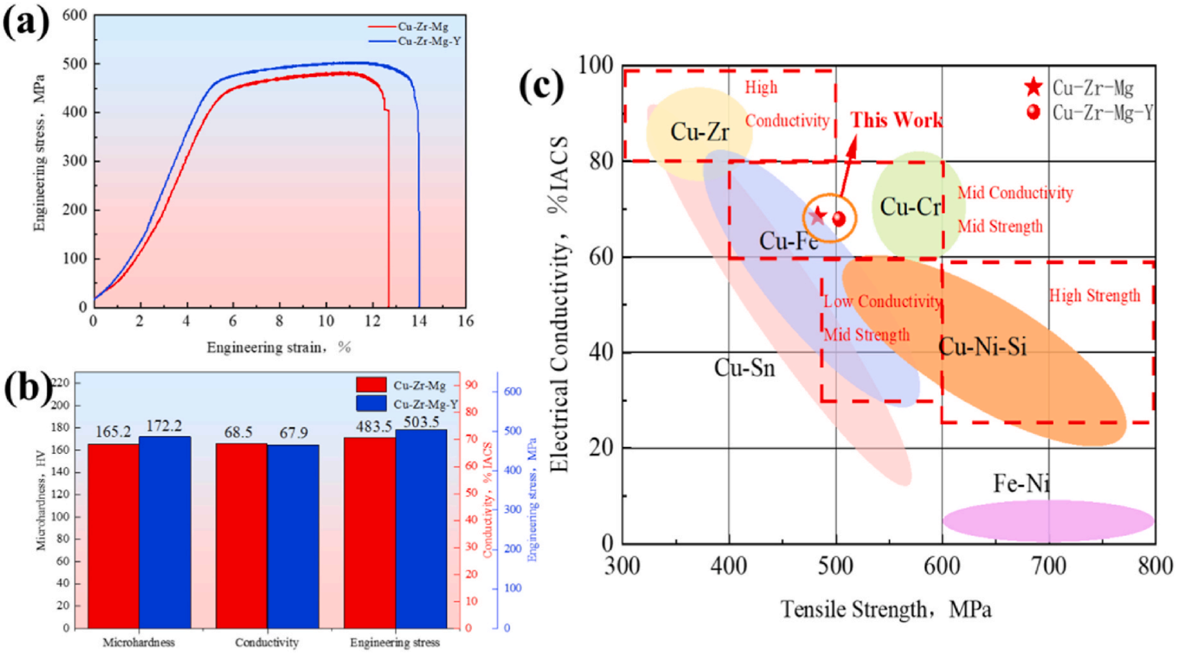

Fig. 5. (a) the curve of tensile strength at peak aging; (b) the comparison of microhardness, tensile strength, and electrical conductivity; (c) the comparison of the properties with the current common copper alloy for lead frame.

Meanwhile, for the Cu-1.2Zr-0.3Mg-0.15Y alloy, these values were 172 ± 6 HV, 67.9 ± 0.2 % IACS, and 503 ± 12 MPa.

The comparison results of properties between Cu-Zr-Mg and Cu-Zr-Mg-Y alloys are depicted in Fig. 5(b). The addition of Y resulted in an increment in microhardness of 7 HV and tensile strength of 20 MPa and only a slight reduction in electrical conductivity, amounting to 0.6 % IACS. Further comparison with a traditional copper alloy used for lead frames is presented in Fig. 5(c) [35]. The incorporation of Mg and Y into the Cu-Zr alloy evidently enhances its mechanical properties, albeit at the expense of diminished electrical conductivity. In comparison, the incorporation of Mg significantly impacts the conductivity of the alloy. Y, on the other hand, plays a role in impurity removal and matrix purification during melting, reducing the solid solubility of impurity elements and enhancing the electrical conductivity of the matrix. From the figures, it is evident that the mechanical and electrical properties of Cu-Zr-Mg and Cu-Zr-Mg-Y alloys align well, making them suitable choices for copper alloys used in lead frames.

3.3. EBSD analysis

Fig. 6 displays the IPF map and the corresponding grain size statistical map of Cu-Zr-Mg and Cu-Zr-Mg-Y alloys aged for 60 min and 360 min, respectively. As depicted in Fig. 6(a) and (c), in the alloy aged for 60 min, the grain boundaries were not clearly analyzable, and there were a small number of finely recrystallized grains present. This may be attributed to the short aging time, insufficient recrystallization in certain

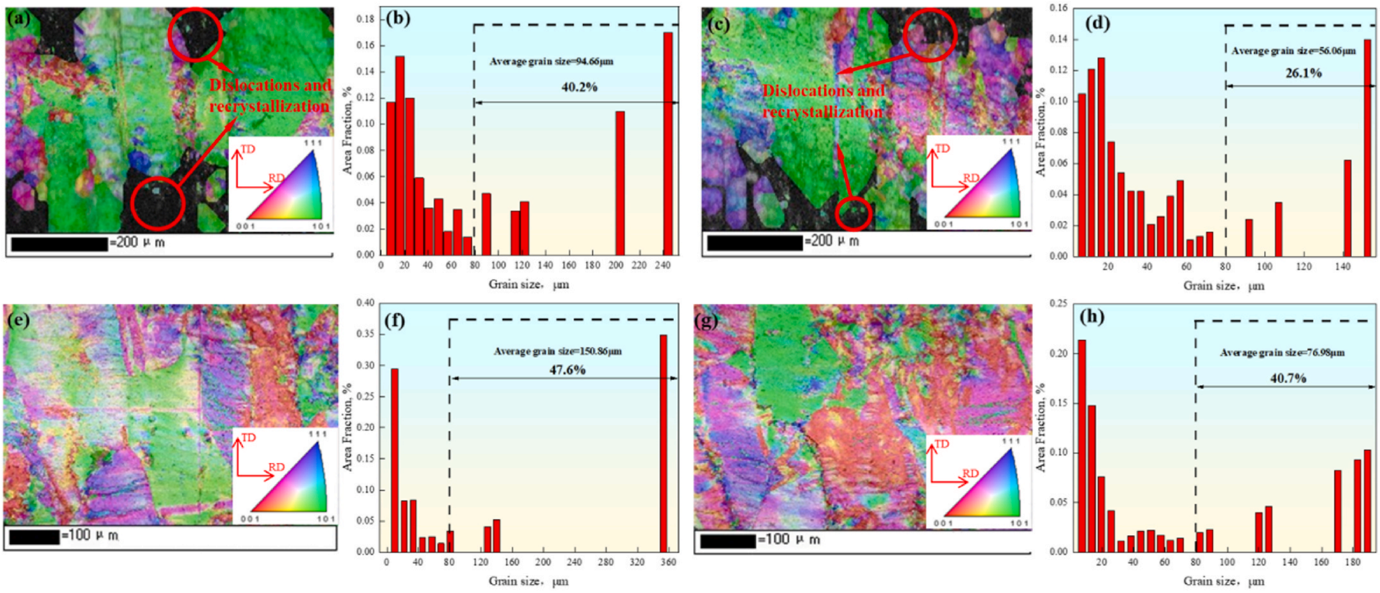

Fig. 6. IPF map and grain size of Cu–Zr–Mg and Cu–Zr-Mg–Y alloys aged at 450 °C: (a) (b) Cu-Zr-Mg alloy aging for 60 min; (c) (d) Cu-Zr-Mg-Y alloy aging for 60 min; (e) (f) Cu-Zr-Mg alloy aging for 360 min; (g) (h) Cu-Zr-Mg-Y alloy aging for 360 min.

areas, and the huge number of dislocations that accumulate at the grain boundaries and within deformation zones. During this period, there are still noticeable large-sized deformed grains in the alloy, with recovery and recrystallization occurring in some regions. The corresponding grain size statistical chart indicates that the maximum grain size in Cu-Zr-Mg alloy is 244.3 μm, grains larger than 80 μm constitute approximately 40.2 % of the total area, and the average grain size is 94.66 μm. Meanwhile, for the Cu-Zr-Mg-Y alloy, the maximum grain size is 152.29 μm, grains larger than 80 μm account for about 26.1 % of the total area, and the average grain size is 56.05 μm. This suggests that the addition of Y promotes recrystallization, resulting in more recrystallized grains and a finer grain size in the Cu-Zr-Mg-Y alloy after 60 min of aging.

The driving force of recrystallization is known to depend on the amount of deformation-stored energy in the alloy. Higher deformation-stored energy facilitates easier recrystallization. Studies by Zhang et al. [36] on Cu-Zr-Ce alloy and Tang [37] on Cu-Ni-Sn-Ti-Cr alloys confirm that the addition of certain elements, such as Ce, can increase the dislocation density and deformation stored energy, promoting recovery and recrystallization. The addition of Y may have a similar effect, leading to more undissolved excess phases in the alloy after solid solution. Consequently, in the same amount of deformation, the Cu-Zr-Mg-Y alloy accumulates more deformation stored energy, providing more nucleation points for recrystallization, and is more prone to recovery and recrystallization.

In Fig. 6(e) and (g), with an extended aging time of 360 min, defects become less evident, recrystallized grains predominantly replace deformed grains, and some grains have grown. The average grain size at this point for Cu-Zr-Mg and Cu-Zr-Mg-Y alloys is 150.86 μm and 76.98 μm, respectively. Even during the over-aging stage, the addition of Y results in finer grains, possibly due to the formation of compounds with a high melting point at the grain boundaries by Y, hindering the migration of large-angle grain boundaries and delaying the growth of recrystallized grains.

The KAM maps of the two alloys, aged for 60 min, are shown in Fig. 7 (a) and (d), indicating that the Cu-Zr-Mg-Y alloy exhibits a lower dislocation density. Internal strain can be discerned through the geometric necessary dislocation density (GND) [38,39]. According to Fig. 7 (b) and (e), the GND of Cu-Zr-Mg and Cu-Zr-Mg-Y alloys aged for 60 min is 6.5×10^{13} m^{-2} and 6.1×10^{13} m^{-2}, respectively. The GND of the Cu-Zr-Mg-Y alloy decreased by 7 %, indicating a higher consumption of dislocations in the alloy. Fig. 7(c) and (f) depict the misorientation angle distribution of the two alloys aged for 60 min. Generally, a higher proportion of recrystallized grains results in finer grains and a greater content of high-angle grain boundaries (HAGBs >15°). From the above figures, it can be observed that the high-angle grain boundary of the Cu-Zr-Mg alloy accounts for 22.7 %, while the high-angle grain boundary of the Cu-Zr-Mg-Y alloy accounts for 27.6 %. The lower GND value and the higher proportion of HAGBs also support the assertion that Cu-Zr-Mg-Y alloy is more susceptible to recovery and recrystallization when the aging time is 60 min.

Fig. 8 shows the pole figures, ODF maps, and comparison diagram of the main texture component of the two alloys aged for 60 min. In the two alloys, the component of cube and goss texture is less, and the volume fraction is 1.38 %, 2.46 % and 8.92 %, 5.68 %, respectively. The component of brass texture is greater, and the volume fraction is 46.1 % and 27.5 %, respectively. No matter whether cold deformation or hot deformation, metals will generally generate texture [40], Sidor et al. [41] believe that for low stacking fault energy metals such as copper alloys (SFE $<$ 25 mJm^{-2}) usually generate strong {1 1 0}<1 1 2> textures, and the weaving of the τ-fiber orientation in the ODF map, corresponds to the brass and copper textures in the figure. In terms of texture types, the biggest difference between the two alloys is the difference in copper texture component. The ODF map displays the texture components of the two alloys with texture strengths exceeding 10 mud. Cu-Zr-Mg-Y alloy has more copper texture than Cu-Zr-Mg alloy. This may be one of the reasons why the Cu-Zr-Mg-Y alloy has a higher tensile strength.

3.4. TEM analysis

To further elucidate the strengthening mechanism of the alloy, we opted for TEM analysis on the Cu-Zr-Mg-Y alloy. Fig. 9 shows TEM and HRTEM images of Cu-Zr-Mg-Y alloy aged at 450 °C for 60 min. The presence of precipitates in Fig. 9 (a) has been observed to impede the movement of dislocations, resulting in the formation of dislocation loops surrounding the precipitates. The preliminary analysis suggests that the precipitation-strengthening process can be attributed to the Orowan mechanism. In addition, the precipitation of atoms from solid solutions reduces the extent of electron scattering and lattice deformation in the matrix, thereby indirectly enhancing the electrical conductivity of the alloy [42]. The sample exhibits a multitude of dislocations, which intertwine to form dislocation walls, thereby enhancing the strength of

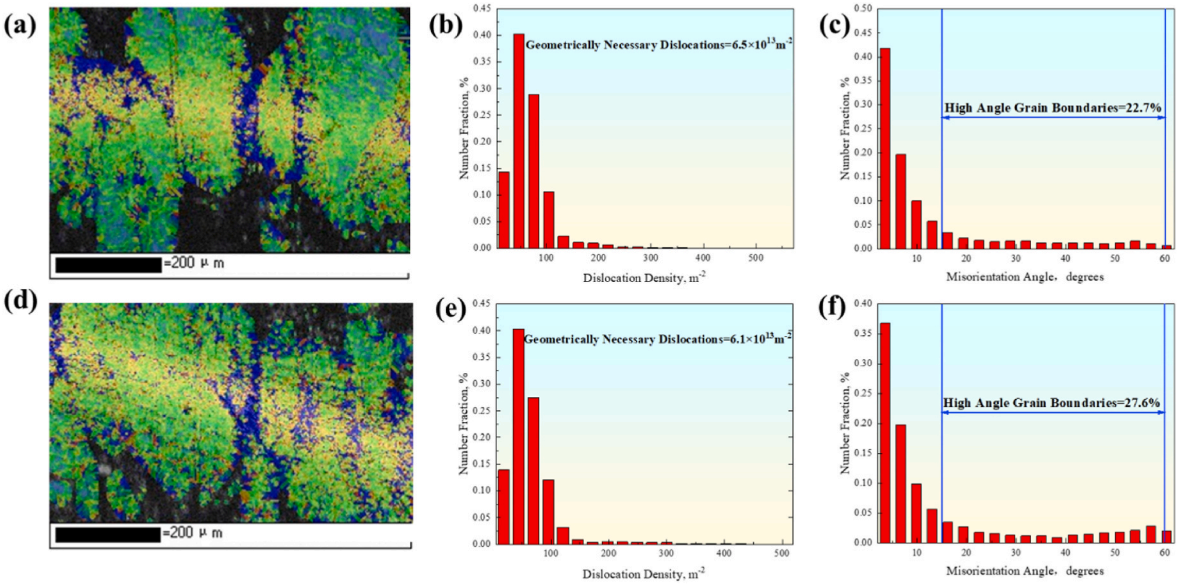

Fig. 7. KAM map, GND map and misorientation angle of Cu–Zr–Mg and Cu– Zr-Mg–Y alloys aged at 450 °C for 60 min: (a) (b) (c) Cu–Zr–Mg alloys; (d) (e) (f) Cu–Zr–Mg-Y alloy.

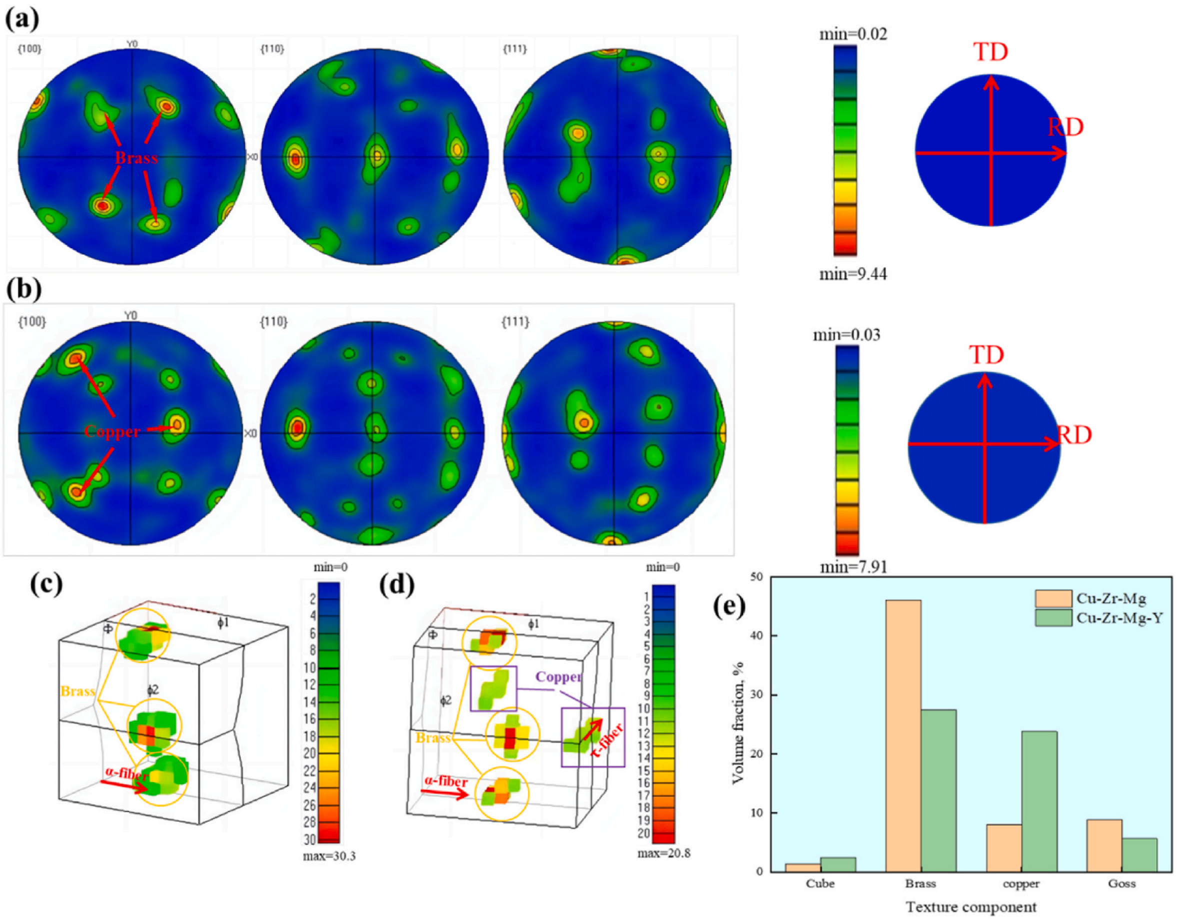

Fig. 8. pole figure, ODF figure and texture component statistical diagram of Cu-Zr-Mg and Cu-Zr-Mg-Y alloys aged for 60 min: (a) (c) Cu-Zr-Mg alloy; (b) (d) Cu-Zr-Mg-Y alloy; (e) texture component statistical diagram.

the alloy. It can be seen from Fig. 9 (b) that there are many precipitates with a size of 6–10 nm in the matrix. To ascertain the kind of precipitates and their orientation in relation to the copper matrix, Fig. 9 (c) displays the HRTEM picture of the copper matrix taken from the [110] direction. The precipitated phase of nanometer size is Cu_5Zr, which is the main strengthening phase and has a cubic structure, the lattice parameter is a = b = c = 0.687 nm, α = β = γ = 90°. From the FFT image in Fig. 9 (d), the presence of an orientation relationship between Cu_5Zr and the copper matrix is evident, which can be expressed as $(200)_{Cu} \parallel (400)_{Cu5Zr}$, $(111)_{Cu} \parallel (222)_{Cu5Zr}$, $(1\bar{1}\bar{1})_{Cu} \parallel (2\bar{2}\bar{2})_{Cu5Zr}$ and $[110]_{Cu} \parallel [110]_{Cu5Zr}$. The mismatch strains between the interfaces are 4.5 %, 4.9 % and 4.9 %, respectively. The crystal structure model of Cu_5Zr is shown in Fig. 9 (e). The coherent interface can enhance the strength of the alloy while preserving its plasticity [43]. In addition, a small quantity of precipitates, about 10–20 nm in size, were found in the alloy, which were calibrated as $Mg_{24}Y_5$, with a cubic structure and lattice parameter of a = b = c = 1.12 nm, α = β = γ = 90°. The orientation relationship between $Mg_{24}Y_5$ and the copper matrix is shown in Fig. 9 (g) (h), which can be expressed as $(111)_{Cu} \parallel (2\bar{2}\bar{4})_{Mg24Y5}$, $[110]_{Cu} \parallel [110]_{Mg24Y5}$. The mismatch between two parallel planes is 9.2 %, which is a semi-coherent relationship. The crystal structure model of Cu_5Zr is shown in Fig. 9 (i). The contribution of this phase to the strength of the alloy was evaluated through geometric phase analysis (GPA). As shown in Fig. 9 (j), on the $(2\bar{2}\bar{4})$ plane, the presence of a significant compressive stress in close proximity to the two-phase interface is clearly evident, indicating that this precipitate also plays a role in precipitation strengthening.

In the Cu-Zr-Mg-Y alloy, continuous and interlaced deformation twins with a width of about 5 nm, along with larger annealing twins, were identified. The results are presented in Fig. 10(a)–(c). Fig. 10(b)–(d), (e) reveal that in the copper alloy, the predominant twins are Sigma3 twins, with the [112] plane serving as the symmetry axis. The increased occurrence of twins leads to the introduction of a greater number of grain boundaries, thereby contributing to the refinement of grains [44]. Yu et al. [45] argue that twins generally have low dislocation density, facilitating the reduction of strain in the alloy. Moreover, an abundance of twin boundaries impedes dislocation movement, collectively enhancing both the strength and plasticity of the alloy.

Fig. 10(f) focuses on the region with a misorientation angle less than 1° within the green-framed area in Fig. 10(e), denoted by the blue part. It is evident that there is minimal misorientation within the twins, signifying low strain. This lower local stress and increased grain boundaries within the twins make twin strengthening more effective than traditional grain boundary strengthening, potentially improving both strength and plasticity. Ban et al. [46] posit that structures featuring multiple layers of interlaced twins (DTS and DTS) can further subdivide the interior of grains, restrict the movement of dislocations to the nanometer region, and induce the Hall-Petch effect caused by twins. In comparison with traditional grain boundary strengthening, the strengthening effect attributed to twins can result in higher plasticity for the alloy. The coherent and semi-coherent precipitates, dislocation cells formed by dislocation entanglement, and nano-sized deformation twins collectively contribute to the excellent mechanical properties of the Cu-Zr-Mg-Y alloy.

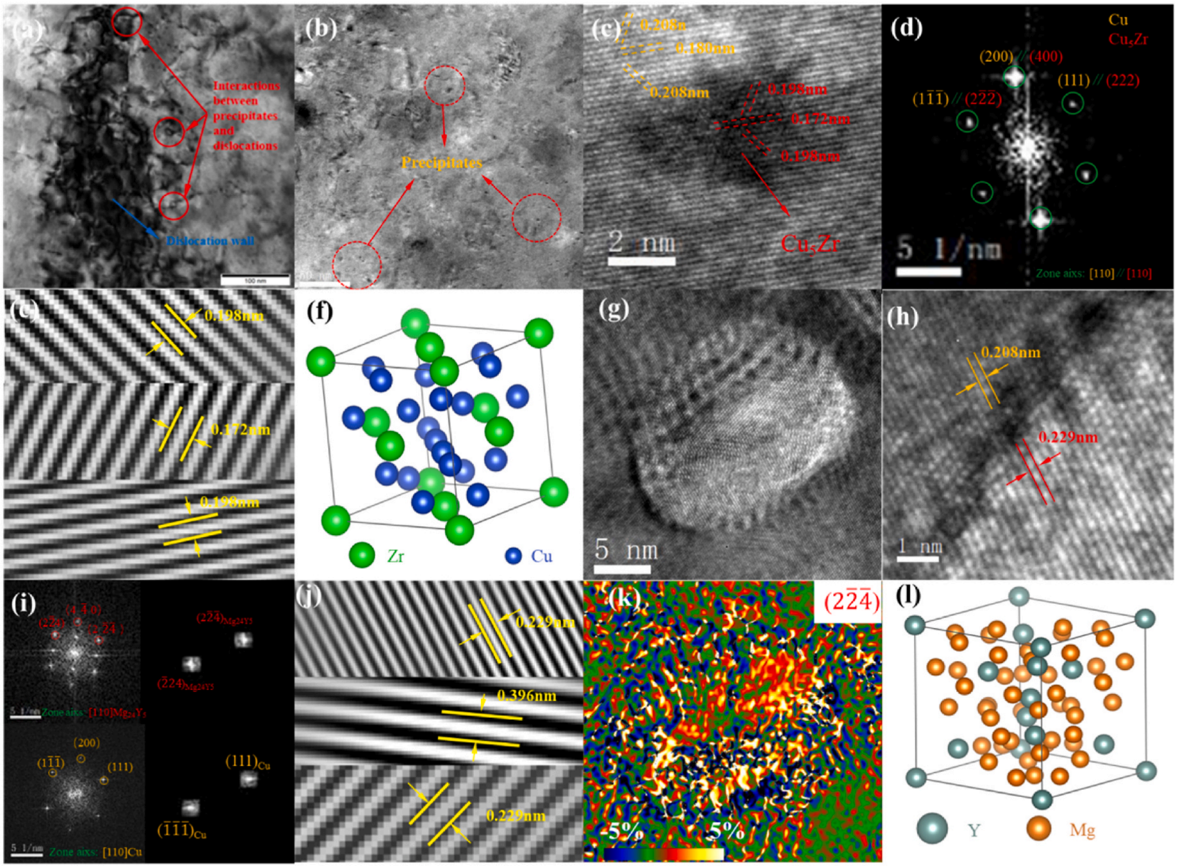

Fig. 9. TEM map of Cu-Zr-Mg-Y alloy aged at 450 °C for 60min: (a) (b) BF image; (c) HRTEM image taken from Cu[110]; (d) FFT image of (c); (e) IFFT image of (c); (f) crystal structure model of Cu_5Zr; (g) HRTEM image taken from Cu[110]; (h) partial enlarged image in the green box of (g); (i) FFT image of (g); (j) IFFT image of (a); (k) The strain distributions around the $Mg_{24}Y_5$ in the specimen calculated by GPA for $(2\bar{2}\bar{4})$ plane; (f) crystal structure model of Cu_5Zr.

4. Discussion

4.1. Effect of Y addition on microstructure and properties of Cu-Zr-Mg alloy

Fig. 11(a) illustrates the distribution of deformation, recovery, and recrystallization regions divided by local misorientations of 2° and 15°. The red area represents the deformation zone, the yellow area signifies the recovery zone, and the blue area indicates the recrystallization zone. In Fig. 11(b) and (c), the distribution of brass texture and copper texture is presented. Analysis of these three figures reveals that the brass texture is predominantly found in the deformed grains, while the copper texture is mainly present in the recovered and recrystallized grains. The addition of Y promotes recovery and recrystallization, potentially accounting for the increased occurrence of copper texture in the Cu-Zr-Mg-Y alloy. The impact of texture on mechanical properties primarily lies in anisotropy, where the strength in a specific direction is contingent upon the difficulty of initiating the slip system when force is applied in that direction. This can be assessed using the Schmidt factor (SF) [47]:

$$\tau = P\cos\theta/A_s = P\cos\theta\cos\varphi/A_0 = \sigma\cos\theta\cos\varphi \tag{1}$$

Here, A_0 is any crystal plane, P represents the force applied in the normal direction of A_0, and A_s is the slip plane , θ represents the angle formed by the force axis and the direction of the dislocation slide, φ is the included angle of the slip surface's normal force axis, τ is the critical shear stress in the slip direction, σ is the normal stress on the sliding surface. The calculation method of the Schmidt factor is shown in Fig. 11 (g). The lower the Schmidt factor, the more challenging it becomes to initiate dislocation slip in this region, consequently leading to an increased tensile strength of the alloy in this direction. The loading direction of the tensile strength previously tested is parallel to the rolling direction. Therefore, the Schmidt factor of the Cu-Zr-Mg-Y alloy is calculated. The results are shown in Fig. 11 (d). When the loading direction is parallel to rolling direction. The Schmidt factor of copper-oriented grains is significantly smaller than that of brass-oriented grains. Fig. 11 (e) (f) shows the distribution of the Schmidt factor inverse pole figure of the {111}<110> slip system of FCC metal according to the Schmidt factor formula and the actual distribution of the Schmidt factor inverse pole figure. The concurrence between the outcomes of the simulation and the empirical results is apparent. The orientation of the copper texture is {112}<111>. The orientation of the brass texture is {011}<112>. This indicates that when the rolling direction and the loading direction are parallel. The direction of the force axis at the copper texture is parallel to the <111> direction, while brass is parallel to the <112> direction. According to Fig. 11(e) (f), the Schmidt factor of the force axis parallel to the <111> direction is significantly lower than that parallel to the <112> direction. It means that when we conduct tensile strength tests parallel to the rolling direction, Cu-Zr-Mg-Y alloys with more copper-oriented grains have lower Schmidt factors, and higher tensile strength. In conclusion, the inclusion of Y promotes the recovery and recrystallization of the alloy, leading to a transformation of the initial deformed grains from a brass texture to a copper texture. Finer grains and more copper texture may be one of the reasons why Cu-Zr-Mg-Y alloy has higher plastic toughness and tensile strength than Cu-Zr-Mg alloy.

4.2. Strengthening mechanisms

The strengthening mechanism of the alloy primarily encompasses

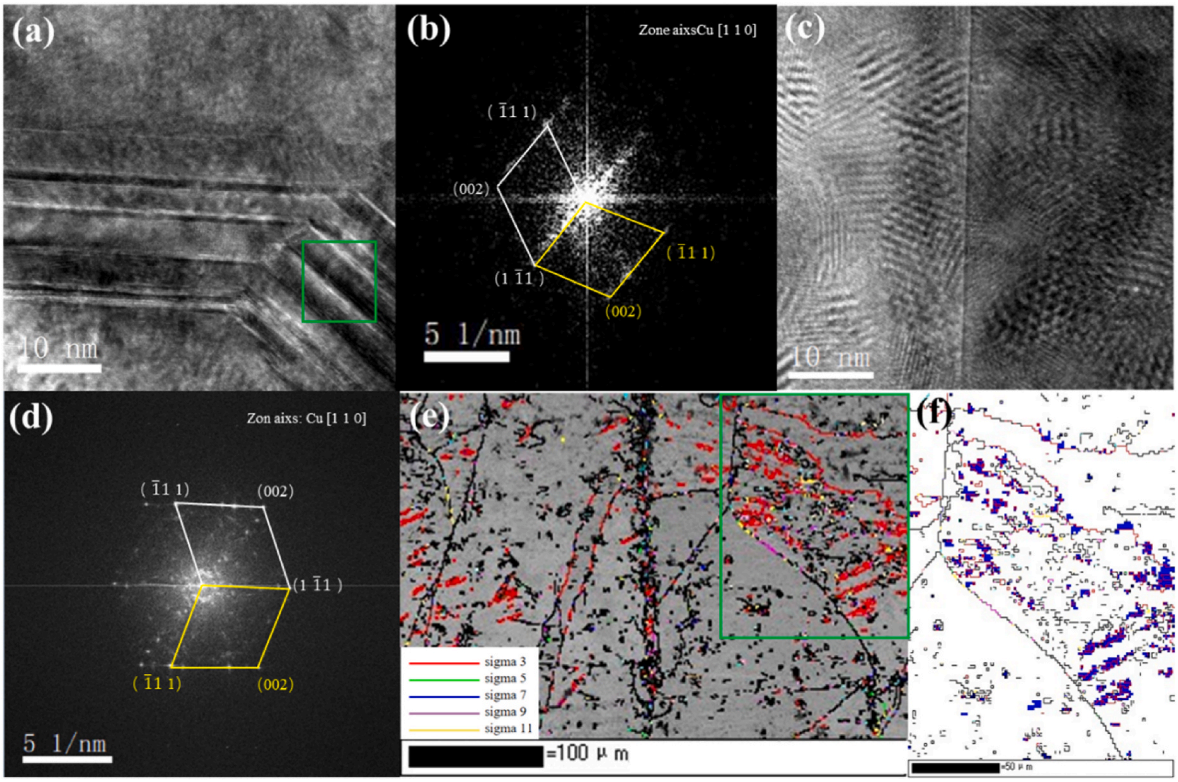

Fig. 10. TEM images of Cu-Zr-Mg-Y alloy aged at 450 °C for 60 min: (a) (c) HRTEM images taken from Cu[110]; (b) FFT image in the green box of (a); (d) IFFT image of (c); (e) twin distribution image (f) Partial enlarged area of (e).

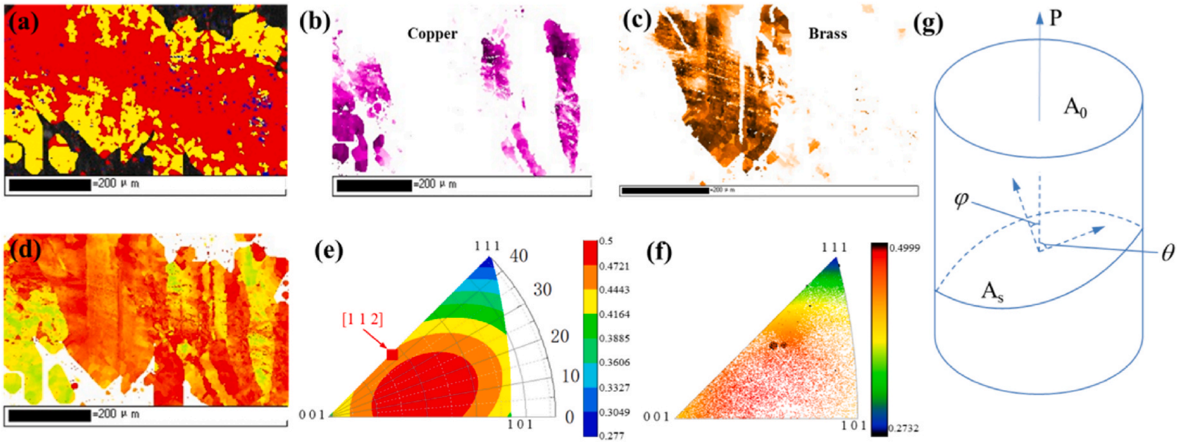

Fig. 11. Distribution of (a) recovery and recrystallization regions of Cu-Zr-Mg-Y alloy aged for 60 min; (b) (c) copper, brass texture distribution; (d) Schmidt factor map; (e) calculated Schmidt factor IPF map; (f) Schmidt factor IPF map of (d); (g) schematic diagram of Schmidt factor calculation method.

solution strengthening, dislocation strengthening, grain boundary strengthening, and precipitation strengthening. Cu-Zr alloys fall under aging-strengthening alloys, exhibiting a robust precipitation strengthening effect. The influence of solution strengthening on the yield strength of Cu-Zr-Mg-Y alloy can be disregarded from a conductivity perspective. The electrical conductivity of the alloy is highly sensitive to the percentage of precipitate volume, which contributes significantly to its overall behavior, as Matthiesen's rule indicates that the alloy's resistivity and solute atom fraction have a linear connection [48]. The volume fraction of precipitates exhibits a correlation with the electrical conductivity of the alloy:

$$f_p=(C-C_0)/(C_{max}-C_0) \tag{2}$$

Here, C is the current electrical conductivity of the alloy, and the alloy's electrical conductivity prior to aging is denoted by C_0, the alloy's electrical conductivity tends to remain stable at a value known as C_{max}. From the perspective of electrical conductivity, the electrical conductivity of the Cu-Zr-Mg-Y alloy aged for 60 min has been nearly stable, f_p is approximately equal to 1, showing that the solid solution atoms are almost completely precipitated. Therefore, the yield strength of the alloy mainly comes from the dislocation strengthening provided by the dislocation formed by cold deformation, the grain boundary strengthening provided by recrystallization during aging, and the precipitation strengthening generated by the formation of coherent and semi-coherent precipitates with the matrix :

$$\sigma=\sigma_0+\sigma_{ds}+\sigma_{GB}+\sigma_p \tag{3}$$

Here, σ_0 is the copper matrix's yield strength, about 20 MPa [49], the strength that comes from work-hardening is represented by σ_{ds}; the stress caused by the strengthening of grain boundaries is represented by σ_{GB}, precipitation strengthening stress is represented by σ_p.Therefore, we can determine which strengthening method is the main strengthening method by calculating each strengthening method's contribution to the yield strength of the alloy.

The increase in yield strength provided by work hardening can be expressed as in Ref. [50] :

$$\sigma_{ds} = M\alpha Gb\sqrt{\rho} \tag{4}$$

Here, M is the Taylor factor, M = 3.06, α is geometric constant, $\alpha = 0.3$, G is the shear modulus of copper matrix, G = 46 GPa, b is the Burke vector of the copper alloy, b = 0.2556 nm, ρ is geometrically necessary dislocation density, $\rho = 6.1 \times 10^{13}\ \mathrm{m}^{-2}$. The work hardening process is anticipated to result in an enhancement of 86 MPa in the yield strength.

The Hall-Petch formula can be utilized to articulate the augmentation in grain boundary reinforcement [51,52]:

$$\sigma_{GB} = K_y {d_g}^{-1/2} \tag{5}$$

Here, K_y is the Hall-Petch coefficient, $K_y = 150\ \mathrm{MPa}\ \mu\mathrm{m}^{1/2}$, d_g is the average grain size, $d_g = 56.05\ \mu\mathrm{m}$, it can be calculated that the increase in grain boundary strengthening provided by work hardening is about 86 MPa.

Due to the large size and less distribution of the $Mg_{24}Y_5$ phase, it can be assumed that precipitation strengthening mainly depends on a significant amount of finely divided Cu_5Zr phase. According to the phenomena observed in TEM and relevant references [53], the Orowan-Ashby equation can be used to determine the increase in yield strength provided by precipitation [54].:

$$\sigma_p = 0.81 \times \frac{MGb}{2\pi(1-\upsilon)^{1/2}} \times \frac{\ln\left(d_p/b\right)}{(\lambda - d_p)} \tag{6}$$

Here, M is the Taylor factor for the fcc matrix [55], M = 3.06, G is the shear module of copper alloy, G = 46 GPa [56], b is the Burgers vector of copper alloy, b = 0.2556 nm, ν is the Poisson's ratio, ν=0.34, d_p is the average size of precipitates, λ is the spacing between particles in the glide plane, which is able to be stated as:

$$\lambda = \frac{1}{2} d_p \sqrt{\frac{3\pi}{2f_p}} \tag{7}$$

Here, f_p stands for the precipitate volume fraction, In this paper, d_p and f_p are obtained by counting the size and number of precipitates in multiple low magnification TEM bright field images. $d_p = 6.4$ nm, $f_p = 1.4$ %. The precipitation strengthening mechanism results in an approximate increase of 313 MPa in yield strength. Finally, it can be determined that the Cu-Zr-Mg-Y alloy has a yield strength of about: $\sigma = \sigma_0 + \sigma_{ds} + \sigma_p + \sigma_{GB} = 20 + 86 + 20 + 313 = 439$ MPa. Compared with the experimentally determined tensile strength of the Cu-Zr-Mg-Y alloy (460 MPa), it is about 4 % lower. This may be due to ignoring the solid solution strengthening provided by a small part of solid solution atoms and the precipitation strengthening provided by a small number of large-size $Mg_{24}Y_5$ precipitates not being calculated. The yield strength increase provided by this part is about 14 MPa. The increase in yield strength provided by various strengthening effects is shown in Fig. 12. The figure shows that the greatest increase in yield strength comes from precipitation strengthening, accounting for 72.4 % of all yield strength increases.

5. Conclusions

(1) Cu-Zr-Mg and Cu-Zr-Mg-Y alloys with favorable mechanical and electrical properties were prepared using vacuum melting and by incorporating multiple metal elements and controlling the aging parameters.

(2) The results reveal that the optimal aging parameter for the two alloys is 60 min at 450 °C the Cu-Zr-Mg and Cu-Zr-Mg-Y alloys have microhardness, electrical conductivity, and tensile strength of 165 ± 5 HV, 483 ± 15 MPa, 68.5 ± 0.2 % IACS, and 172 ± 6 HV, 503 ± 12 MPa, 67.9 ± 0.2 % IACS, respectively. The mechanical properties of Cu-Zr-Mg alloy were enhanced by the addition of Y, with increasing the microhardness of 7 HV and the tensile strength of 20 MPa, respectively, while the electrical conductivity did not decrease significantly.

(3) The addition of Y promotes the recovery and recrystallization of the alloy, results in the generation of finely recrystallized grains that enhance the tensile strength and plasticity of the alloy. The Cu-Zr-Mg-Y alloy presents higher tensile strength. When the tensile strength test is conducted parallel to the rolling direction, the copper texture is predominant in the recovered and recrystallized grains, may contribute to the higher tensile strength.

(4) Several mechanisms are suitable to explain the increament of mechanical properties of Cu-Zr-Mg-Y alloy, including dislocation, grain boundary, and precipitate. The formation of a significant quantity of coherent Cu_5Zr precipitation and a minor amount of

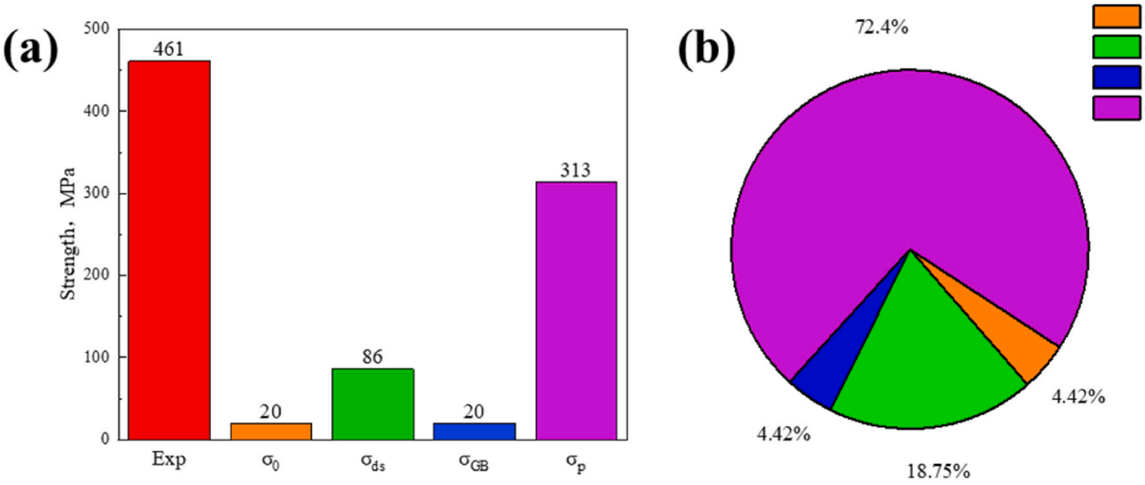

Fig. 12. Yield strength increment provided by various strengthening mechanisms of Cu-Zr-Mg-Y alloy aged at 450 °C for 60min: (a) statistical chart; (b) proportion chart.

semi-coherent Mg$_{24}$Y$_5$ precipitation is the main factor responsible for the alloy’s exceptional mechanical and electrical properties. The existence of numerous precipitates reduces the content of solid solution atoms in the copper matrix, decreases electron scattering and significantly improves the electrical conductivity. Simultaneously, a lattice mismatch between these precipitates and the matrix interface hinders dislocation movement, results in notable precipitation strengthening. The formation of abundant nano twins refines the grain structure and enhances the alloy’s plasticity due to the low stress within the twins.

(5) The increase of yield strengthcaused by dislocation, grain boundary, and precipitate are 86 MPa, 20 MPa, and 313 MPa, respectively. The mian strengthening source is precipitate, which accounts for 72.4 % of the total yield strength increment.

CRediT authorship contribution statement

Haoyan Hu: Writing – review & editing, Writing – original draft, Methodology, Formal analysis, Conceptualization. **Meng Zhou:** Resources, Project administration. **Xu Li:** Investigation. **Yi Zhang:** Writing – review & editing, Funding acquisition. **Qian Bai:** Formal analysis. **Bo Yang:** Formal analysis. **Jin Zou:** Supervision, Resources. **Ke Jing:** Supervision, Resources. **Zheng’ao Li:** Formal analysis. **Gang’ao Xin:** Formal analysis. **Baohong Tian:** Supervision, Resources. **Alex A. Volinsky:** Writing – review & editing.

Declaration of competing interest

The authors declare that they have no known competing financial interests or personal relationships that could have appeared to influence the work reported in this paper.

Data availability

Data will be made available on request.

References

[1] W. Wang, Z. Xiao, Q. Lei, H. Meng, Q. Guo, Y. Yang, Z. Li, A multiphase strengthened Cu-Nb-Si alloy with high strength and high conductivity, Mater. Char. 182 (2021) 111565.
[2] W. Chen, X. Hu, W. Guo, J. Zou, K. Liu, D. Lu, D. Tan, Effects of C Addition on the microstructures of as-cast Cu-Fe-P alloys, Materials 12 (2019) 2772.
[3] J. Yang, K. Bu, Y. Zhou, K. Song, T. Huang, X. Peng, H. Liu, Y. Du, Microstructure, residual stress, and mechanical properties evolution of a Cu-Fe-P alloy under different conditions, J. Mater. Res. Technol. 24 (2023) 7896–7909.
[4] B. Wang, Y. Zhang, B. Tian, Y. Jia, A.A. Volinsky, V. Yakubov, Y. Liu, K. Song, M. Fu, Nanoscale precipitates evolution and strengthening mechanism of the aged Cu-Mg-Fe-Sn-P-Y electrical contact wire, J. Mater. Res. Technol. 9 (2020) 6352–6359.
[5] Y. Ma, Q. Lei, J. Xu, Y. Liang, X. Meng, Y. Li, Z. Xiao, Effects of Zn addition on the microstructure and properties of Cu-Cr alloys, Mater. Sci. Technol. 39 (2023) 1914–1925.
[6] M. Ma, Z. Xiao, X. Meng, Z. Li, S. Gong, J. Dai, H. Jiang, Y. Jiang, Q. Lei, H. Wei, Effects of trace calcium and strontium on microstructure and properties of Cu-Cr alloys, J. Mater. Sci. Technol. 112 (2022) 11–23.
[7] V. Fotopoulos, C.S. O’Hern, M.D. Shattuck, A.L. Shluger, Modeling the effects of varying the Ti concentration on the mechanical properties of Cu-Ti alloys, ACS Omega 9 (2024) 10286–10298.
[8] X. Wang, Y.-j. Ding, X.-f. Jiang, X.-p. Meng, Z. Xiao, Effects of Fe content on properties and microstructure of Cu–Ti alloys during aging, J. Mater. Res. Technol. 27 (2023) 5518–5532.
[9] Z. Zhao, Z. Li, Z. Xiao, M. Ma, K. Song, Dynamic recrystallization of Cu-Cr-Ni-Si-Co alloy during hot deformation, J. Miner. Met. Mater. Soc. 73 (8) (2021) 2274–2284.
[10] J. Yi, Y. Jia, Y. Zhao, Z. Xiao, K. He, Q. Wang, M. Wang, Z. Li, Precipitation behavior of Cu-3.0Ni-0.72Si alloy, Acta Mater. 166 (2019) 261–270.
[11] K. Jha, S. Neogy, S. Kumar, R.N. Singh, G.K. Dey, Correlation between microstructure and mechanical properties in the age-hardenable Cu-Cr-Zr alloy, J. Nucl. Mater. 546 (2021) 152775.
[12] K. Nakashima, K. Miyamoto, T. Kunimine, R. Monzen, N. Muramatsu, Precipitation behavior of Cu-Zr compounds in a Cu-0.13 wt%Zr alloy, J. Alloys Compd. 816 (2020) 152650.
[13] Q. Liu, X. Zhang, Y. Ge, J. Wang, J.-Z. Cui, Effect of processing and heat treatment on behavior of Cu-Cr-Zr alloys to railway contact wire, Metall. Mater. Trans. A 37 (2006) 3233–3238.
[14] Y. Ban, Y. Zhang, B. Tian, K. Song, M. Zhou, X. Zhang, Y. Jia, X. Li, Y. Geng, Y. Liu, A.A. Volinsky, EBSD analysis of hot deformation behavior of Cu-Ni-Co-Si-Cr alloy, Mater. Char. 169 (2020) 110656.
[15] P. Liu, B.X. Kang, X.G. Cao, J.L. Huang, B. Yen, H.C. Gu, Aging precipitation and recrystallization of rapidly solidified Cu-Cr-Zr-Mg alloy, Mater. Sci. Eng. 265 (1999) 262–267.
[16] L. Arnberg, U. Backmark, N. Bäckström, J. Lange, A new high strength, high conductivity Cu-0.5wt.%Zr alloy produced by rapid solidification technology, Mater. Sci. Eng. 83 (1986) 115–121.
[17] A. Kauffmann, D. Geissler, J. Freudenberger, Thermal stability of electrical and mechanical properties of cryo-drawn Cu and CuZr wires, Mater. Sci. Eng. 651 (2016) 567–573.
[18] K. Yamaguchi, Y.-C. Song, T. Yoshida, K. Itagaki, Thermodynamic investigation of the Cu-Zr system, J. Alloys Compd. 452 (2008) 73–79.
[19] M. Azimi, G.H. Akbari, Development of nano-structure Cu-Zr alloys by the mechanical alloying process, J. Alloys Compd. 509 (2011) 27–32.
[20] H. Kimura, H. Matsumoto, A. Inoue, Effect of cold drawing on electrical and mechanical properties of Cu-5 at% Zr alloy, Mater. Trans. 48 (2007) 2674–2678.
[21] J. Deng, X. Zhang, S. Shang, F. Liu, Z. Zhao, Y. Ye, Effect of Zr addition on the microstructure and properties of Cu-10Cr in situ composites, Mater. Des. 30 (2009) 4444–4449.
[22] J. Huang, Z. Xiao, J. Dai, Z. Li, H. Jiang, W. Wang, X. Zhang, Microstructure and properties of a novel Cu-Ni-Co-Si-Mg alloy with super-high strength and conductivity, Mater. Sci. Eng. 744 (2019) 754–763.
[23] Y. Sun, L. Peng, G. Huang, H. Xie, X. Mi, X. Liu, Effects of Mg addition on the microstructure and softening resistance of Cu-Cr alloys, Mater. Sci. Eng. 776 (2020) 139009.
[24] Z. Zhao, Z. Xiao, Z. Li, M. Ma, J. Dai, Effect of magnesium on microstructure and properties of Cu-Cr alloy, J. Alloys Compd. 752 (2018) 191–197.
[25] S.G. Mu, F.A. Guo, Y.Q. Tang, X.M. Cao, M.T. Tang, Study on microstructure and properties of aged Cu-Cr-Zr-Mg-RE alloy, Mater. Sci. Eng. 475 (2008) 235–240.
[26] J. Su, P. Liu, H. Li, F. Ren, Q. Dong, Phase transformation in Cu-Cr-Zr-Mg alloy, Mater. Lett. 61 (2007) 4963–4966.
[27] R. Monzen, C. Watanabe, Microstructure and mechanical properties of Cu–Ni–Si alloys, Mater. Sci. Eng. 483–484 (2008) 117–119.
[28] B. Wang, Y. Zhang, B. Tian, V. Yakubov, J. An, A.A. Volinsky, Y. Liu, K. Song, L. Li, M. Fu, Effects of Ce and Y addition on microstructure evolution and precipitation of Cu-Mg alloy hot deformation, J. Alloys Compd. 781 (2019) 118–130.
[29] X. Chen, Q. Li, Y. Zhou, P. Chen, Creep behavior and creep mechanism of Mg-Gd-Y-Sm-Zr alloy, Vacuum 212 (2023) 112009.
[30] H. Wan, B. Xu, B. Yang, J. Zhao, Y. Dai, The impurities distribution and purification efficiency of high-purity aluminum preparation by zone melting in vacuum, Vacuum 171 (2020) 108839.
[31] J. Chu, Y. Bao, Study on the relationship between vacuum denitrification and manganese evaporation behaviours of manganese steel melts, Vacuum 192 (2021) 110420.
[32] M.N. Mathabathe, A.S. Bolokang, G. Govender, R. Mostert, C.W. Siyasiya, The vacuum melted ɣ-TiAl (Nb, Cr, Si)-doped alloys and their cyclic oxidation properties, Vacuum 154 (2018) 82–89.
[33] W. Chen, X.N. Hu, J. Zou, W. Guo, D.P. Lu, D.Q. Tan, Refinement effect of C addition on the Cr phase in the as-cast Cu–Cr alloys, Vacuum 179 (2020) 109485.
[34] K. Abiko, S. Takaki, Ultra-purification of iron by ultra-high vacuum melting, Vacuum 53 (1–2) (1999) 93–96.
[35] S. Xie, Y. Li, L. Zhu, Progress of study on lead frame copper alloy and its implementation in electronic industry, Rare Met. 27 (2003) 769.
[36] Y. Zhang, H. Sun, A.A. Volinsky, B. Wang, B. Tian, Y. Liu, K. Song, Constitutive model for hot deformation of the Cu-Zr-Ce alloy, J. Mater. Eng. Perform. 27 (2018) 728–738.
[37] S. Tang, M. Zhou, Y. Zhang, D. Xu, Z. Zhang, X. Zheng, D. Li, X. Li, B. Tian, Y. Jia, Y. Liu, A.A. Volinsky, E.S. Marchenko, Improved microstructure, mechanical properties and electrical conductivity of the Cu-Ni-Sn-Ti-Cr alloy due to Ce micro-addition, Mater. Sci. Eng. 871 (2023) 144910.
[38] Y. Wu, X. Qin, C. Wang, L. Zhou, Influence of phosphorus on hot deformation microstructure of a Ni-Fe-Cr based alloy, Mater. Sci. Eng. 768 (2019) 138454.
[39] Y. Wu, Z. Liu, X. Qin, C. Wang, L. Zhou, Effect of initial state on hot deformation and dynamic recrystallization of Ni-Fe based alloy GH984G for steam boiler applications, J. Alloys Compd. 795 (2019) 370–384.
[40] L. Bracke, K. Verbeken, L. Kestens, J. Penning, Microstructure and texture evolution during cold rolling and annealing of a high Mn TWIP steel, Acta Mater. 57 (2009) 1512–1524.
[41] J.J. Sidor, L.A.I. Kestens, Analytical description of rolling textures in face-centred-cubic metals, Scripta Mater. 68 (2013) 273–276.
[42] S. Nagarjuna, K. Balasubramanian, D.S. Sarma, Effect of prior cold work on mechanical properties, electrical conductivity and microstructure of aged Cu-Ti alloys, J. Mater. Sci. 34 (1999) 2929–2942.
[43] L. Lu, Y. Shen, X. Chen, L. Qian, K. Lu, Ultrahigh strength and high electrical conductivity in copper, Science 304 (2004) 422–426.
[44] S. Picak, J. Liu, C. Hayrettin, W. Nasim, D. Canadinc, K. Xie, Y.I. Chumlyakov, I. V. Kireeva, I. Karaman, Anomalous work hardening behavior of Fe40Mn40Cr10Co10 high entropy alloy single crystals deformed by twinning and slip, Acta Mater. 181 (2019) 555–569.

[45] Y. Fu, W. Xiao, D. Kent, M.S. Dargusch, J. Wang, X. Zhao, C. Ma, Ultrahigh strain hardening in a transformation-induced plasticity and twinning-induced plasticity titanium alloy, Scripta Mater. 187 (2020) 285–290.

[46] Y. Ban, Y. Geng, J. Hou, Y. Zhang, M. Zhou, Y. Jia, B. Tian, Y. Liu, X. Li, A. A. Volinsky, Properties and precipitates of the high strength and electrical conductivity Cu-Ni-Co-Si-Cr alloy, J. Mater. Sci. Technol. 93 (2021) 1–6.

[47] X.-L. Nan, H.-Y. Wang, L. Zhang, J.-B. Li, Q.-C. Jiang, Calculation of Schmid factors in magnesium: analysis of deformation behaviors, Scripta Mater. 67 (2012) 443–446.

[48] C. Xia, Y. Jia, W. Zhang, K. Zhang, Q. Dong, G. Xu, M. Wang, Study of deformation and aging behaviors of a hot rolled-quenched Cu-Cr-Zr-Mg-Si alloy during thermomechanical treatments, Mater. Des. 39 (2012) 404–409.

[49] M. Gholami, J. Vesely, I. Altenberger, H.-A. Kuhn, M. Janecek, M. Wollmann, L. Wagner, Effects of microstructure on mechanical properties of CuNiSi alloys, J. Alloys Compd. 696 (2017) 201–212.

[50] Z. Wang, W. Lu, H. Zhao, C.H. Liebscher, J. He, D. Ponge, D. Raabe, Z. Li, Ultrastrong lightweight compositionally complex steels via dual-nanoprecipitation, Sci. Adv. 6 (2020) eaba9543.

[51] Y. Zhang, N.R. Tao, K. Lu, Mechanical properties and rolling behaviors of nano-grained copper with embedded nano-twin bundles, Acta Mater. 56 (2008) 2429–2440.

[52] N. Hansen, Hall-Petch relation and boundary strengthening, Scripta Mater. 51 (2004) 801–806.

[53] L. Peng, H. Xie, G. Huang, Y. Li, X. Yin, X. Feng, X. Mi, Z. Yang, The phase transformation and its effects on properties of a Cu-0.12 wt% Zr alloy, Mater. Sci. Eng. 633 (2015) 28–34.

[54] M. Mabuchi, K. Higashi, Strengthening mechanisms of Mg-Si alloys, Acta Mater. 44 (1996) 4611–4618.

[55] Q. Lei, Z. Li, Z. Pan, M. Wang, Z. Xiao, C. Chen, Dynamics of phase transformation of Cu-Ni-Si alloy with super-high strength and high conductivity during aging, Trans. Nonferrous Metals Soc. China 20 (2010) 1006–1011.

[56] X. Guo, Z. Xiao, W. Qiu, Z. Li, Z. Zhao, X. Wang, Y. Jiang, Microstructure and properties of Cu-Cr-Nb alloy with high strength, high electrical conductivity and good softening resistance performance at elevated temperature, Mater. Sci. Eng. 749 (2019) 281–290.